Acta of Bioengineering and Biomechanics
Vol. 27, No. 3, 2025

Original paper
DOI: 10.37190/abb/210576

Role of wall compliance and cushioning in the fluid–structure interaction study of a high-flow artery

DANIEL M. JODKO*

Institute of Turbomachinery, Lodz University of Technology, Łódź, Poland.

Purpose: Fluid–structure interaction (FSI) techniques have become widely accepted numerical tools for analysing transient flows through compliant channels and tubes. However, FSI remains computationally demanding and requires assumptions about certain parameters that are often difficult to determine, particularly in biomedical applications. This study aimed to demonstrate the importance of key decisions required to conduct FSI simulations. *Methods*: Appropriate material properties were selected and parameters that define the magnitude of external reactions and cushioning effects (which are usually unknown but can be discovered through reverse engineering were set). Using a simplified model of an elastic straight tube, which represents a high-flow artery, reduced the influence of shape and associated mesh imperfections on the results. *Results*: Wall deformation, von Mises stress, wall shear stress and the pressure drop along the tube were analysed. Verification with various mesh densities for the compliant wall demonstrated that mesh fidelity significantly affects von Mises stress and computation time on a standard PC but has a negligible effect on wall deformation, wall shear stress and pressure drop. *Conclusions*: Varying wall stiffness and foundation stiffness affected the resulting compliance and all monitored parameters. Additionally, applying different mass and stiffness coefficients to define Rayleigh damping identified a safe range of applicability of this type of damping, however, experimental validation is necessary to determine appropriate values for specific applications and avoid overdamping. Finally, the results were discussed in the context of other FSI research and relevant in vivo and in vitro blood flow studies.

Key words: *pulsatile flow, fluid–structure interaction, foundation stiffness, Rayleigh damping, cushioning effect, large artery*

1. Introduction

Over the last 20 years, two-way coupled fluid–structure interaction (FSI) simulations have been commonly employed as a numerical technique to model multiphysics problems efficiently [11]. FSI considers the mutual influence of flowing fluid and surrounding or immersed structures. Such commercial or in-house developed partitioned FSI tools enable the simultaneous work of two distinct solvers, which parallelly resolve equations governing computational fluid dynamics (CFD) and structural mechanics, usually using finite volume and finite element methods. Stress, force or displacement information is exchanged between solvers via a defined interface, therefore, the fluid and structure domains must have a geometric match. However, despite the quick development of high-speed computers with constantly accelerated processors, FSI simulations are still time-consuming compared to traditional CFD using a rigid-wall approach. The long time necessary to obtain results is associated with calculations and the inevitability of preparing two numerical domains, including two numerical grids. As numerical grid-based methods are time-consuming, newer approaches, such as meshless non-linear dynamics combined with FSI calculations, accelerated by graphic processing units or using monolithic methods [3], are being developed. In the monolithic approach, a large nonlinear system that simultaneously handles both fluid and structural dynamics is solved as a single coupled problem, but it can be challenging to implement. It is worth mentioning

* Corresponding author: Daniel M. Jodko, Institute of Turbomachinery, Łódź University of Technology, Łódź, Poland, e-mail: daniel.jodko@p.lodz.pl

Received: July 9th, 2025
Accepted for publication: September 10th, 2025

that in numerical studies, an alternative one-way approach has also been used, however, it is based on static equations, neglecting the inertia of walls and does not provide the time evolution of the stress distribution [7].

As computer simulations are currently a widely accepted tool in conducting research in the area of biomedical engineering and biomechanics, FSI is becoming a commonly used approach in modelling pulsatile blood flows. Starting from simplified or idealised models of arteries [27], the FSI approach has been used to investigate hemodynamics in patient-specific models with complex geometrical shapes. Good examples of such a personalised approach, including FSI, can be found among various parts of the cardiovascular system, like the largest human artery, the aorta [40], carotid arteries [14], coronary arteries [12], cerebral aneurysms [25], pulmonary arteries [17], and arteriovenous fistulas [13] with the abnormal blood flow in the anastomosis region (in which the artery is sutured to the vein). Several papers put a special emphasis on FSI modelling in pathological arterial stenoses [14]. FSI was used in modelling the human heart pressure-volume operation [28]. Further, FSI was successfully used in modelling blood flow around flexible membranes of the total artificial heart [36] and has high potential for developing cardiovascular medical devices, such as stents. However, due to the complicated geometry of the wire coils forming stent grafts deployed in patient-specific blood vessels, to model the blood flow through such stents, the rigid-wall approach has typically been chosen [10] or only structural solvers could be used to model the process of stent deployment [4].

In the above-mentioned FSI studies, blood vessel walls were treated as one-layered. A modification of this type of modelling is using multi-layered walls, which is intended to be more realistic as arterial walls are composed of three main layers: intima, media and adventitia [24]. Sandeep and Shine presented FSI modelling, which takes into account a multi-layered simplified structure of coronary stenosis with additional consideration of plaque [32]. Therefore, there is a question concerning the benefits of using time-consuming FSI in modelling blood flows through elastic tubes simulating parts of the human circulatory system, which is built of compliant soft tissues. Especially since in numerous studies based on computer simulations of blood flows, patient-specific blood vessel geometries have been considered to be rigid [2]. Similar doubts are raised in experimental works using stiff physical phantoms created with rapid-prototyping methods, sometimes followed by a moulding process [9]. Some researchers used resilient *in vitro* models made of silicon [19], latex [26], or elastic polymers [15]. Thus, it is worth knowing if the effort spent on creating such phantoms is profitable.

In this paper, the significance of key assumptions in 2-way FSI simulations using a compliant tube representing a generic model of a large artery characterised by a high flow-to-diameter ratio is highlighths. This approach provides a benchmark test, as no geometrical factors were investigated. The sensitivity analysis was done using a standard PC and may be useful for researchers in the cardiovascular field. The FSI results were compared against those obtained with a rigid wall model. Additionally, unsuccessful simulations (negative results) were described to emphasise the difficulties of FSI modelling.

2. Materials and methods

A simplified and idealised model of an artery was created to show a representative FSI simulation of the arterial blood flow. Additionally, we assumed the high flow scenario and considerable pressure change within a cardiac cycle that can occur, e.g., in the artery feeding an arteriovenous fistula (AVF) for hemodialysis, the common carotid artery, or the femoral artery. Blood flow in such arteries can exceed 400 ml/min. In the presented case, the inlet mean blood flow is equal to 8.21 cm^3/s (493 ml/min), which is recalculated from the applied velocity profile and its changes over time.

2.1. Fluid and wall geometry, wall fixation and stabilisation, wall damping, and model of compliance

The entire geometrical model is presented in Fig. 1a. The fluid domain is a circular tube with a diameter of 6 mm and a length of 150 mm. A separate structural domain representing the wall was created, for which a thickness of 0.5 mm was assumed. The ending cross--sections of the structure were considered to be motionless to define the tube's position in space. The linear material model, described by Young's modulus (E), was employed for the wall. Numerous models have been developed to model arterial wall behaviour. However, even for the simplest, linear one, different values of Young's modulus have been used in the literature. Thus, in the present study, a few values of Young's modulus were compared: $E = \{0.5, 1, 3\}$ MPa (for the rigid model, it can be assumed that $E = \infty$). The range of 0.5–3 MPa encompasses commonly used values [14], [18], [37]. The Poisson's ratio was assumed to be equal to 0.45 in all FSI simulations.

The mechanical response of the loose connective tissue (LCT) surrounding the artery was modelled by the stabilisation of the wall, which was represented by the Robin boundary condition [8], defined by the foundation stiffness coefficient (FS). The magnitude of this reaction is unknown and difficult to measure *in vivo* [35], thus several different values of FS were assumed: FS = {0 (no support), 0.01, 0.1, 0.5} N/mm^3. Such method was employed in a patient-specific carotid FSI modelling in [14] and a similar approach, in which FS = k = 0.01 N/mm^3, was used by Guess for patient-specific AVF [8]. This mechanical response can be understood as the stiffness of a spring acting on a unit external surface of the artery model in a direction perpendicular to the wall.

As two-way FSI modelling was performed here, cushioning effects were taken into account with the employment of the Rayleigh damping described by the mass and the stiffness coefficients, which are symbolised, respectively, by α and β. These constants are crucial in dynamic analyses; however, it is difficult to determine them for real objects [29]. Damping is usually neglected in the literature devoted to the FSI in the cardiovascular area, and a limited number of papers provide such information. In Jodko et al. [14] FSI blood flow simulations in a patient-specific carotid branch were obtained only for the relation $\alpha = \beta = 0.01$. Zhu et al. used $\alpha = 50$ and $\beta = 0.1$ in the FSI study of the aorta [40]. In practical cases, it is also recommended to ignore alpha damping. Therefore, as Rayleigh damping still seems an unsolved issue in FSI blood flow modelling, different values and combinations of α and β were used in this study.

2.2. Fluid, boundary conditions, and assumptions

The idealised parabolic velocity profile was applied: $V_p = V_{\max}\,[1 - (r/R_{\max})^2]$ as the inlet boundary condition in the fluid domain. The maximal velocity is a time function ($V_{\max} = V_{\max}(t)$) and is applied at the inlet centre and is assumed to be a function of time. Radius r is the radial coordinate in the plane of the inlet, and $R_{\max} = 3$ mm is the radius of the tube. $V_{\max}(t)$ was read from *in vivo* measurements done by Wiese et al. [38] with an ultrasound technique in the artery feeding a properly working mature AVF. Some researchers found that arterial blood flow can be disturbed despite a low Reynolds number [22], [34]. To decide which flow regime, laminar or turbulent, should be taken into account in this study, the turbulent velocity profile was also tested: $V_p = V_{\max}\,[1 - (r/R_{\max})^{1/n}]$ with

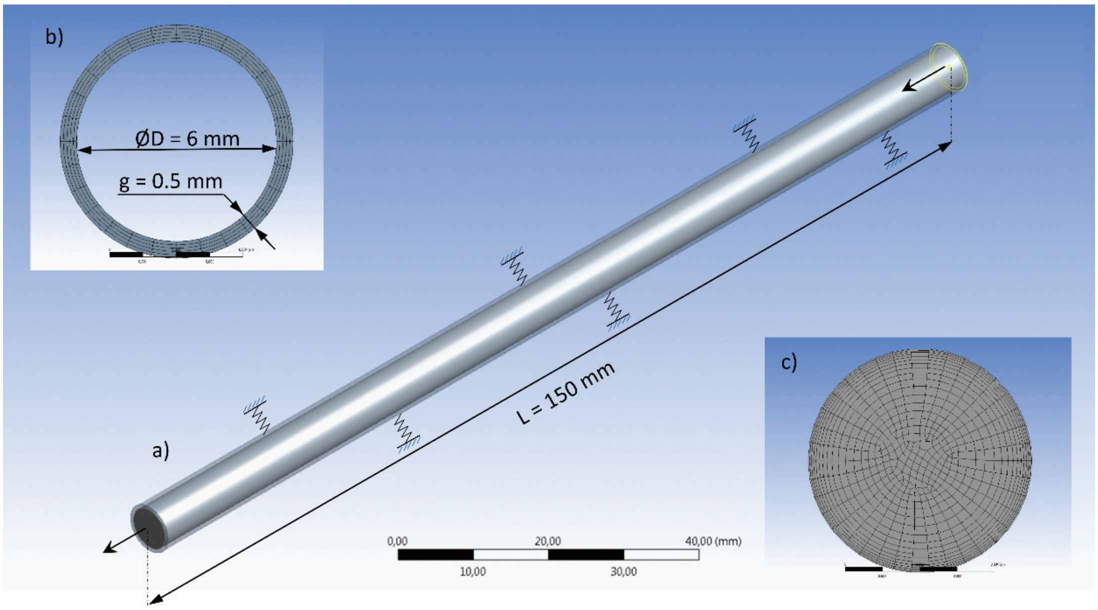

Fig. 1. Fluid and structural domains prepared: a) entire domain of the artery,
b) example of structural mesh (5-element-layered) including 28840 finite elements in the wall,
c) fluid mesh including 202101 finite volumes used in all the performed simulations;
springs represent external stabilisation and mechanical response of the loose connective tissue (LCT)
that was modelled with elastic support, which is defined by the foundation stiffness coefficient (FS)
and is applied over the entire external surface of the wall

n = 6. However, the mean Reynolds number calculated for the inlet cross-section from $Re = 4\rho Q/\pi\mu D$ was equal to 604 and 955, respectively, for the laminar and the turbulent profile (Q is the mean flow rate obtained for V_p, ρ = 1040 kg/m^3 is the assumed blood density, μ = 0.003 Pa s is the assumed dynamic viscosity of blood, $D = 2R_{\max}$). Thus, due to the idealised shape of the considered artery (no stenoses, aneurysms, or branches), the laminar flow regime was selected for all the performed simulations. The blood density and viscosity assumed in this study are slightly lower than normal, as hemodialysed patients accumulate a significant amount of water in plasma between subsequent haemodialysis sessions. As dynamic effects are modelled within FSI simulations, the normal blood pressure waveform $p_{\text{out}} = p_{\text{out}}(t)$ was assumed as the outlet boundary condition. As in a real-world blood flow, arterial wall expansion is caused by pressure pulsations; the frequently used zero outlet pressure condition would not be suitable for the FSI approach. The data regarding the changes in blood pressure over time were taken from [16] and were time-integrated with the velocity function $V_{\max}(t)$ to maintain a single heart cycle of 0.84 s, corresponding to 71.4 beats per minute. However, three identical cycles were modelled, and the results were extracted only from the last one to avoid the influence of initial conditions. Finally, as arteries are located in deeper parts of the human forearm, heat transfer was not considered.

2.3. Calculations and coupling

The well-established Arbitrary Lagrangian–Eulerian (ALE) method for interface matching in partitioned FSI was employed. This approach allows one to model large deflections. The mathematical representation of the modelling performed by the two employed solvers was as follows (adapted from [39]).

Fluid

Unsteady Reynolds-Averaged Navier–Stokes (URANS) equations were solved to compute the fluid motion. Since external forces were omitted, blood was an incompressible fluid and no heat transfer was considered, URANS could be reduced to

$$\nabla . u = 0 , \tag{1}$$

$$\rho\left(\frac{\partial u}{\partial t} + u.\nabla u\right) - \nabla\sigma_b = 0 , \tag{2}$$

where ρ is blood density, u is blood velocity, and σ_b is stress tensor that is related to the strain rate as follows

$$\sigma_b = -p_b I + 2\mu\varepsilon(u) , \tag{3}$$

where p_b – blood pressure field, μ – dynamic viscosity, and $\varepsilon(u)$ – strain rate tensor that is expressed as

$$\varepsilon(u) = \frac{1}{2}(\nabla u + (\nabla u)^T) . \tag{4}$$

As the laminar regime was used, the turbulent (Reynolds) stress component of URANS was omitted. To accelerate transient flow calculations, the result of a steady-state simulation was employed as initial conditions instead of zero conditions. Due to the simplicity of the geometry, convergence was controlled by 1–3 coefficient loops with the fulfilment of the criteria of residual target equal to 10^{-6}. High-resolution and second-order backwards Euler schemes were used.

Structure

The structural motion was governed by

$$\rho_w\left(\frac{\partial v}{\partial t} + (\nabla v)v - g\right) - \nabla.\sigma_w = 0 , \tag{5}$$

where ρ_w is blood vessel wall density, v is structural velocity field, g represents external body forces, and σw is Cauchy stress tensor.

The displacement of the structure d_w, associated with velocity v, can be presented with a common Lagrangian description form as

$$\rho_w\left(\frac{\partial^2 d_w}{\partial t^2}\right) = g + \nabla.\sigma_w . \tag{6}$$

The Newmark time-integration method was employed.

Coupling

The system coupling module was used to couple the fluid and the structural solvers. As the coupling used the staggered approach, pressure determined in the fluid domain was transferred as a loading through the FSI interface, where displacement, stress, and elastic strain were computed in the solid structure. Further, the information about the wall displacement was transferred back to the fluid domain, where remeshing was necessary. The equality of velocity for both sides of the interface was the kinematic constraint. The dynamic constraint required that the stress tensors of the structure and the fluid normal to the interface be equal. This can be noted as

$$u = v , \tag{7}$$

$$\sigma_b n = \sigma_w n . \tag{8}$$

Maximally 10 stepping iterations with a step size of 0.01 s were set to achieve the RMS convergence target equal to 10^{-2}. Such an approach is a compromise between accuracy and the time of calculations.

2.4. Meshes

Due to the simplified geometry, both fluid and structural meshes were generated using the sweep method in ANSYS Mesher, included in the ANSYS Workbench package. As significantly influencing the calculation time, structural grid fidelity and density were investigated more deeply to show their influence on the results of hemodynamic parameters. Thus, 1-element-layered (N_1), 3-element-layered (N_3), and 5-element-layered (N_5) structural meshes containing, respectively, 6592/42584, 17304/86828, and 28840/133140 finite elements/nodes, were generated, and the selected flow parameters obtained for these meshes were compared. The example of the structural mesh containing 5 layers of linear structural elements throughout the wall thickness is presented in Fig. 1b. The element type selection was discussed by Liu and Fletcher [18].

Different numerical grids M1–M6 representing the fluid domain with varying numbers of finite volumes (from 50 434 to 1 189 020) were generated before performing FSI simulations. Then, one grid was selected in the mesh independence test that was performed with the use of rigid-wall simulations (Fig. 3). The dependence of two resultant flow parameters, TAWSS and Δp, on the number of finite volumes was tested. Finally, as giving comparable results with less than 2% of the difference to the finest grid, a mesh M4 consisting of 202 101 finite volumes and 207328 nodes (Fig. 1c), was chosen and used in all the presented rigid-walled and FSI simulations. Additionally, the selected fluid mesh allowed us to obtain the results much faster than the finest one M1 (33 min vs. 2 h 37 min) as well as faster than the mesh M3 (33 min vs. 1 h 23 min) which significantly reduced the time of FSI calculations that were strongly dependent on structural mesh fidelity (Tables 1 and 2). Mesh motion was allowed near the boundaries of the fluid domain in FSI simulations. A single workstation was used for all calculations: Intel Core i7-3930K CPU 3.20 GHz 6 cores Hyper-V, RAMDIMM 1600 MHz 64 GB.

The comparison of the total calculation time of the selected simulation sets, performed using structural meshes N_1–N_5 and fluid mesh M4 with settings E = {0.5–3} MPa and FS = 0, is presented in Table 1. Interestingly, using 1 MPa allowed us to obtain results faster than 3 MPa and 0.5 MPa. In this test, using a 5-element-layered structural mesh extended the calculation time by ca. 3–4 times when compared to the one-layered grid N_1. On the other hand, although the same numerical grids were used (Table 2), the simulations with elastic support (FS ≠ 0, using a constant Young's modulus E = 3 MPa) required more computation time than those without elastic support (FS = 0).

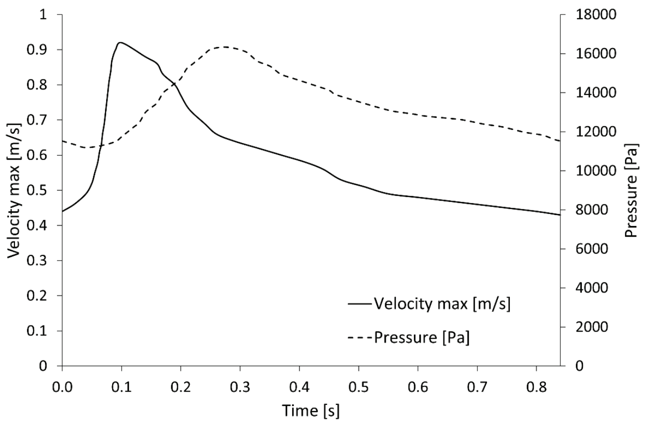

Fig. 2. Inlet and outlet boundary conditions: maximal velocity $V_{max}(t)$ applied at the centre of the inlet and outlet static blood pressure $p_{out}(t)$

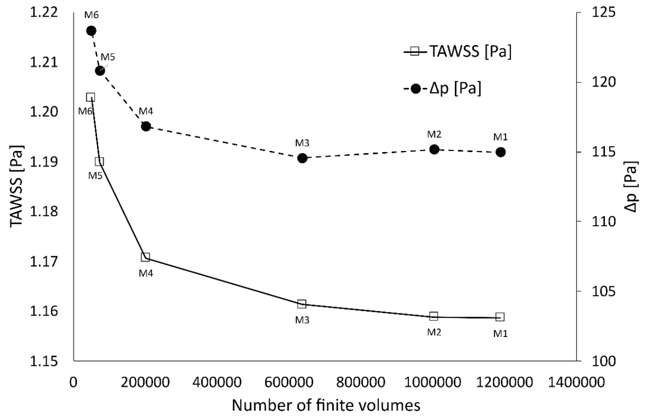

Fig. 3. Fluid mesh tests based on rigid-walled simulations and two parameters characterising the blood flow which were analysed in further FSI simulations; calculation times differ significantly for particular grids: M1 (2 h 37 min), M2 (2 h 6 min), M3 (1 h 23 min, this mesh would be selected in standard CFD analysis), M4 (33 min, the selected mesh that allowed to carry out FSI simulations in reasonable time with acceptable error on the fluid side using the available PC), M5 (20 min), M6 (16 min)

3. Results

The study aimed to show the importance of blood vessel wall compliance in modelling blood flows, thus, FSI simulations were carried out for different meshes

Table 1. Calculation time of selected FSI simulations for different structural meshes N_i and Young's modulus E (for FS = 0, $\alpha = \beta = 0.01$) compared to the rigid-wall simulation time

FSI										Rigid
N_i	1-element-layered (N_1)			3-element-layered (N_3)			5-element-layered (N_5)			
E [MPa]	3	1	0.5	3	1	0.5	3	1	0.5	
Time	6 h 15 min	5 h 26 min	7 h 29 min	18 h 36 min	13 h 43 min	19 h 57 min	1 d 2 h 28 min	21 h 25 min	1 d 1 h 5 min	33 min

Table 2. Calculation time of selected FSI simulations for different structural meshes N_i and elastic support FS (for E = 3 MPa, $\alpha = \beta = 0.01$) compared to the rigid-wall simulation time

FSI													Rigid
N_i	1-element-layered (N_1)				3-element-layered (N_3)				5-element-layered (N_5)				
FS [N/mm^3]	0.5	0.1	0.01	0	0.5	0.1	0.01	0	0.5*	0.1*	0.01*	0	
Time	4 d 20 h 52 min	7 h 30 min	6 h 27 min	6 h 15 min	28 d 19 h 59 min	20 h 14 min	19 h 49 min	18 h 36 min	**	15 h 54 min	16 h 31 min	1 d 2 h 28 min	33 min

* A faster computer station was used in these cases.

** Excluded from further analysis since the calculations were not completed after one month.

and assumptions affecting the wall resilience and the monitored parameters. This approach allows one to compare the obtained results quantitatively, both in the fluid domain (e.g., wall shear stress and pressure drop generated between the inlet and the outlet), and in the structural domain (e.g., mesh displacement and von Mises stress). All the results were extracted only from the third cardiac cycle so that maximal or time-averaged values of the monitored parameters could be determined without the risk of being affected by the initial conditions. Thus, area-averaged wall shear stress averaged over time (TAWSS) and time-averaged pressure drop (Δp) represent a mean flow state, which, as presented later, is dependent not only on the input velocity and pressure waveforms but also on the wall compliance. Since a few factors can be responsible for the level of wall resilience and the dynamics of the mechanical response of the wall to the flow excitation transmitted by pressure, they were investigated separately. Firstly, wall-based compliance, associated with the assumed linear models, was considered without any external support (FS = 0). Secondly, LCT-based resilience was considered and modelled as the mechanical response of LCT using the elastic support at the external wall surface. Finally, various combinations of damping were investigated for the selected compliant model described by E = 3 MPa and FS = 0.

3.1. Dependence on a material model

To investigate elasticity-related wall resilience, several material models describing wall behaviour were compared in this study. Using linear models made it possible to obtain results much faster than the commonly accepted but computationally demanding hyperelastic models, which were developed mainly for modelling larger deformations of rubber-like materials. Moreover, Corpataux et al reported relatively small deformation in the radial artery within the cardiac cycle [5]. Additionally, Torii et al. found that despite the high non-linearity of the experimentally determined relationship between the external radius and inner pressure of a straight pipe representing an artery, for the physiological range of blood pressure, the linear model (E = 1 MPa) almost overlaps the hyperelastic characteristic [37]. Thus, the linear models were assessed as an acceptable simplification, providing inexpensive computations in this study.

The relation between the maximal displacement of the structural mesh and Young's modulus and the number of elements in the wall is shown in Fig. 4; thus, in this set of simulations, other parameters were constant (FS = 0 and $\alpha = \beta = 0.01$). More compliant walls resulted in larger displacements, which was expected. For the most resilient model (E = 0.5 MPa), the maximal mesh deformation was almost 11 times larger than for the least compliant one (E = 3 MPa), regardless of the mesh N_1–N_5. A negligible deviation is visible only for E = 0.5 MPa for the coarsest mesh N_1 when compared to other meshes. For stiffer models, mesh density did not influence the wall extension. This implies that the numerically obtained structural mesh displacement is related mostly to material stiffness and the inner pressure, which in turn is associated with the boundary pressure condition.

Mesh density played a more important role in determining von Mises stress in the structural domain of the wall. In Figure 5, it is shown how the maximal von Mises stress depended on Young's modulus and the number of elements in the wall (for FS = 0 and $\alpha = \beta = 0.01$). A stiffer wall resulted in lower stress, which was expected. The difference in the maximal von Mises stress obtained for cases $E = 0.5$ MPa and $E = 3$ MPa varied from 34% (0.1752 MPa vs 0.1150 MPa) to 15% (0.1775 MPa vs 0.1504 MPa), respectively, for N_1 and N_5. Investigation of the influence of the structural mesh density on von Mises stress showed that, in the considered case, a similar value of the maximal von Mises stress was obtained only for the $E = 0.5$ MPa for all the generated meshes, for which, the difference between the maximal stress obtained for structural meshes (N_5 vs. N_3 vs. N_1) was lower than 2%. Maximal von Mises stress increased for the denser structural grids (N_5 vs. N_1) by

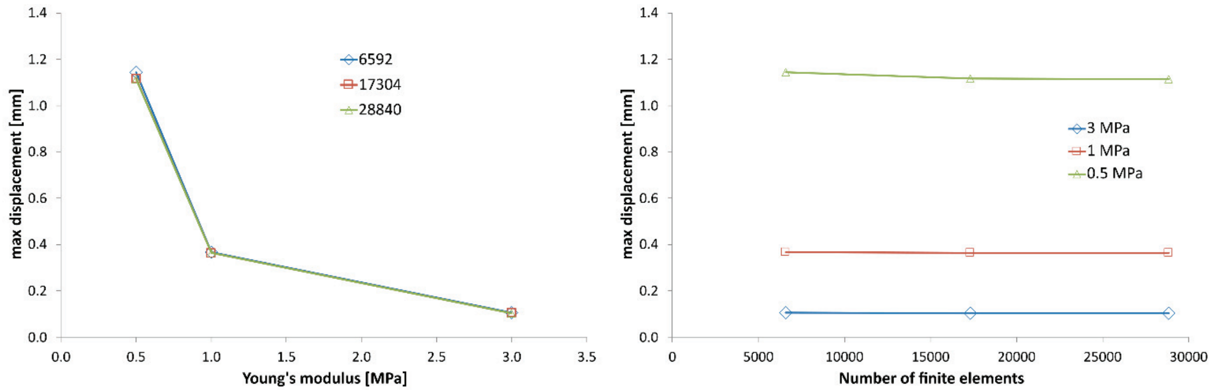

Fig. 4. Left: maximal structural mesh displacement (max displacement) vs. Young's modulus, right: maximal displacement vs. the number of elements in the structure (FS = 0, $\alpha = \beta = 0.01$)

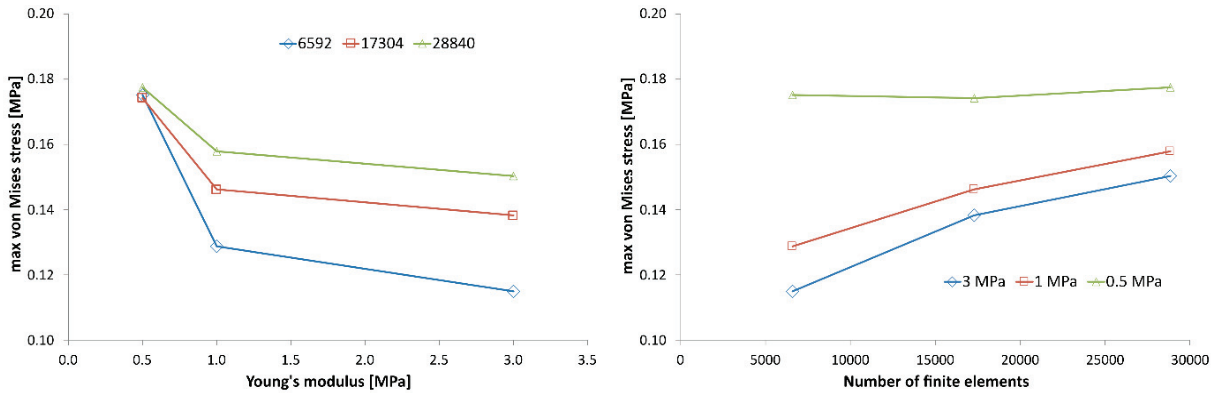

Fig. 5. Left: maximal von Mises stress vs. Young's modulus, right: maximal von Mises stress vs. the number of elements in structure (FS = 0, $\alpha = \beta = 0.01$)

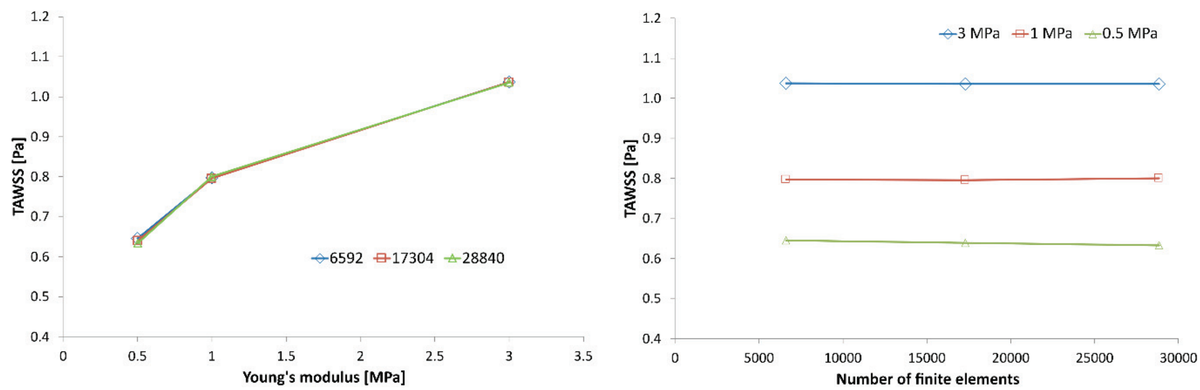

Fig. 6. Left: time-averaged wall shear stress (TAWSS) vs. Young's modulus, right: TAWSS vs. the number of elements in structure (FS = 0, $\alpha = \beta = 0.01$); TAWSS = 1.171 Pa for the rigid model

about 24% (0.1504 MPa vs. 0.1150 MPa) for $E = 3$ MPa and 18% (0.1578 MPa vs. 0.1287 MPa) for $E = 1$ MPa. Thus, precise structural grids should be generated while analysing the stress distribution in the structural domain. Additionally, an acceptable mesh should be selected in the independence test of the grids.

A relation between TAWSS and the used values of Young's modulus and the number of finite elements in the structural domain is presented in Fig. 6. Similarly to wall deformation, TAWSS did not depend on the structural mesh density (less than 2% of the difference between N_5 and N_1). On the other hand, the magnitude of wall shear was associated with the level of wall compliance, as TAWSS was strongly dependent on Young's modulus. For the least resilient models ($E = 3$ MPa), TAWSS was around 1.6 times higher than in the most compliant ones, e.g., 1.0357 Pa vs. 0.6336 Pa for N_5. Although the given example was the most resilient case presented in this study ($E = 0.5$ MPa and FS = 0), this simple test showed the importance of considering wall compliance when analysing wall shear stress. As shown in Table 3, using linear material models resulted in significantly lower TAWSS than in the rigid-wall case. When compared to the rigid model, for which TAWSS = 1.17 Pa, TAWSS extracted from FSI simulations decreased by about 12, 32 and 45%, respectively, for material compliance defined by $E = 3$ MPa, $E = 1$ MPa and $E = 0.5$ MPa.

Although the density of the structural mesh density did not affect the drop in the inlet/outlet pressure and only for $E = 0.5$ MPa and for the structural grid consisting of 28840 elements, Δp was noticeably lower than for the two other meshes (Fig. 7). As shown in Table 4, material-related resilience had a significant impact on the

Table 3. TAWSS [Pa] calculated in FSI simulations for different Young's modulus and structural meshes (FS = 0, $\alpha = \beta = 0.01$) compared to the rigid-wall approach

FSI							Rigid
N_i (number of elements)	3 MPa	3 MPa vs. rigid [%]	1 MPa	1 MPa vs. rigid [%]	0.5 MPa	0.5 MPa vs. rigid [%]	
N_1 (6592)	1.0373	**88.58**	0.7975	**68.10**	0.6451	**55.09**	1.171
N_3 (17304)	1.0360	**88.47**	0.7960	**67.98**	0.6400	**54.65**	
N_5 (28840)	1.0357	**88.45**	0.8000	**68.32**	0.6336	**54.11**	

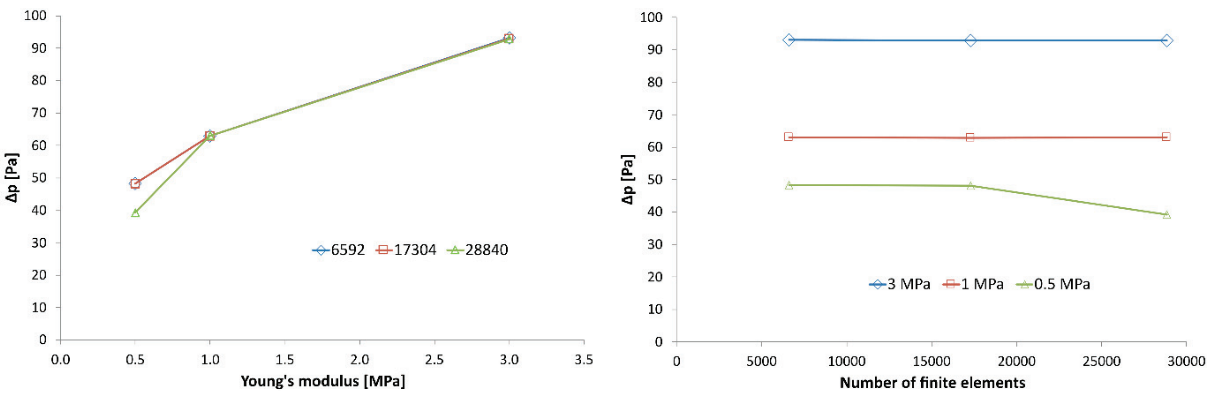

Fig. 7. Left: pressure drop vs. Young's modulus, right: pressure drop vs. number of elements in structure (FS = 0, $\alpha = \beta = 0.01$); $\Delta p = 116.8$ Pa for the rigid model

Table 4. Pressure drop Δp [Pa] calculated in FSI simulations for different Young's modulus and structural meshes (FS = 0, $\alpha = \beta = 0.01$) compared to the rigid-wall approach

FSI							Rigid
N_i (number of elements)	3 MPa	3 MPa vs. rigid [%]	1 MPa	1 MPa vs. rigid [%]	0.5 MPa	0.5 MPa vs. rigid [%]	
N_1 (6592)	93.104	**79.71**	63.024	**53.96**	48.298	**41.35**	116.8
N_3 (17304)	92.932	**79.57**	62.879	**53.83**	48.118	**41.20**	
N_5 (28840)	92.847	**79.49**	62.993	**53.93**	39.288	**33.64**	

pressure drop as Δp was decreased by around 21, 46 and 59–66%, respectively, for $E = 3$ MPa, $E = 1$ MPa, and $E = 0.5$ MPa compared to $\Delta p = 116.8$ Pa obtained in the rigid case. This trend is associated with the increasing accumulation of energy by highly compliant walls.

3.2. Dependence on foundation stiffness

A mechanical response of LCT surrounding blood vessel walls is an independent factor influencing wall resilience. This reaction was modelled using external elastic support, defined by the foundation stiffness coefficient (a few values compared). A constant value of Young's modulus $E = 3$ MPa was arbitrarily chosen to avoid over-deformation that occurred in highly compliant models, for which low E and low FS were considered.

The relation between the maximal displacement of the structural mesh versus FS and the number of elements in the structural grids is shown in Fig. 8. Similarly to the above-mentioned dependence of the mesh displacement on the material properties of the wall, higher stiffness of LCT resulted in lower extension, also in this case. For FS = 0.1/0.01/0 N/mm^3, the density of the structural mesh did not affect the maximal mesh displacement; however, for the least compliant model (FS = 0.5 N/mm^3), mesh distensibility depended on the structural grid. Therefore, the maximal displacement in the most resilient cases (for FS = 0) was 2.6/3.7 times larger, respectively for N_1/N_3, than in the case with FS = 0.5 N/mm^3 (N_5 excluded from further analysis since the calculation time exceeded one month).

As shown in Fig. 9, foundation stiffness influenced the maximal von Mises stress, which is lower when the resilience of the surrounding tissues rises. There was no significant difference in the maximal stress between the cases in which FS = 0 and FS = 0.01 N/mm^3 (3.2–5.5% of the difference for all the meshes N_1–N_5). However, using higher values of FS raises the difference, which can reach about 55% when the cases with FS = 0.5 N/mm^3 and FS = 0 are compared for all the meshes (the case including FS = 0.5 N/mm^3 and mesh N_5 was excluded). For the presented cases, finer meshes provided larger maximal von Mises stress; thus, time-demanding mesh independence tests, including denser structural grids, should be performed to determine the stress more ade-

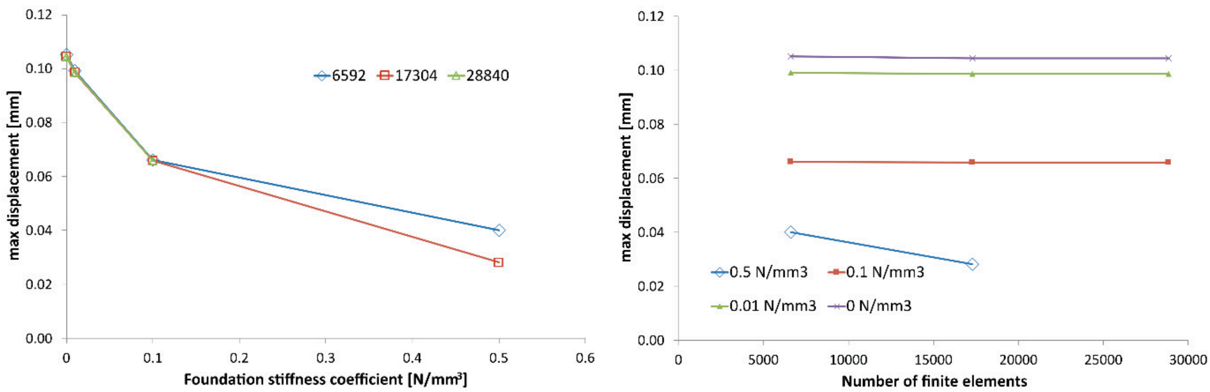

Fig. 8. Left: maximal displacement vs. FS, right: maximal displacement vs. the number of elements in structure ($E = 3$ MPa, $\alpha = \beta = 0.01$), the case including FS = 0.5 N/mm^3 and mesh N_5 was excluded

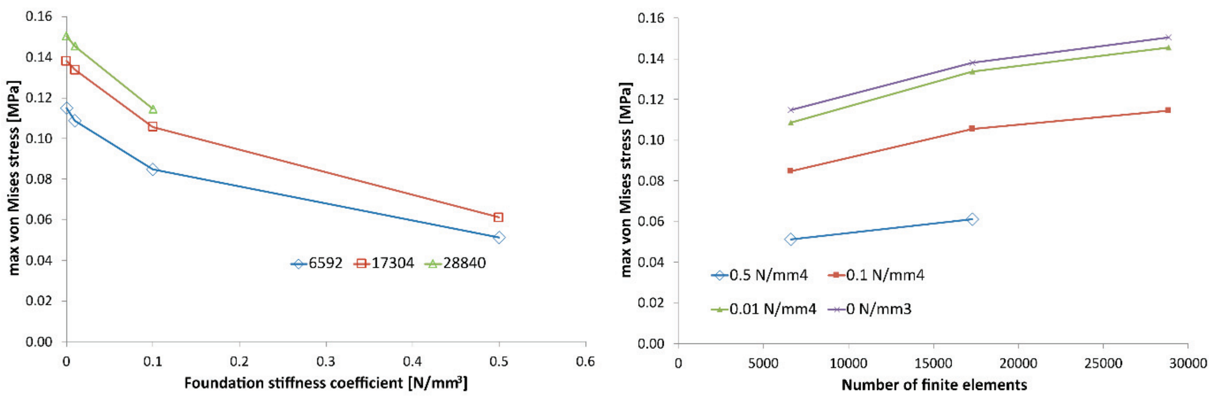

Fig. 9. Left: maximal von Mises stress vs. FS, right: maximal von Mises vs. the number of elements in structure ($E = 3$ MPa, $\alpha = \beta = 0.01$), the case including FS = 0.5 N/mm^3 and mesh N_5 was excluded

quately. However, mechanical stress analysis was not the aim of this study.

As presented in Fig. 10, the lower value of FS, the lower TAWSS, which was by about 3, 7, 10 and 11% lower than in the rigid case (1.171 Pa), respectively, for FS = 0.5/0.1/0.01/0 N/mm^3 (Table 5). As the constant value E = 3 MPa was used in this test, the differences could be higher for lower values of Young's modulus, which would allow the wall for the larger extension. This concerns especially the case without any external support (FS = 0). Such a coincidence of E = 1 MPa and FS = 0 has been reported in the FSI study of a patient-specific carotid bifurcation [14], which, when compared to a rigid-wall analogous model, delivered a higher discrepancy in wall shear (35%). However, in this study, there were no meaningful discrepancies in TAWSS among all the generated structural meshes. This allows us to state that the structural mesh density is not crucial in determining WSS on the fluid side, however, the FSI approach itself is worth consideration as the total model compliance affects the results obtained.

Δp versus FS and the number of elements in the structural grid is presented in Fig. 11. Similarly to the previous set of simulations, in these cases, the structural mesh density does not influence Δp significantly.

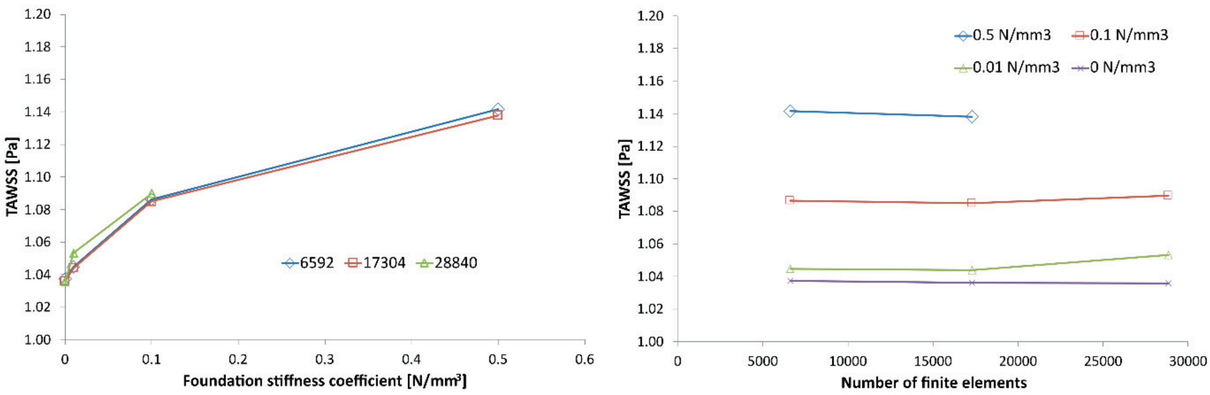

Fig. 10. Left: TAWSS vs. FS, right: TAWSS vs. the number of elements in structure (E = 3 MPa, $\alpha = \beta = 0.01$), TAWSS = 1.171 Pa for the rigid model, the case including FS = 0.5 N/mm^3 and mesh N_5 was excluded

Table 5. TAWSS [Pa] calculated in FSI simulations for different values of the foundation stiffness coefficient and structural meshes (E = 3 MPa, $\alpha = \beta = 0.01$) compared to the rigid-wall approach

FSI									
N_i (number of elements)	0.5 N/mm^3	0.5 N/mm^3 vs. rigid [%]	0.1 N/mm^3	0.1 N/mm^3 vs. rigid [%]	0.01 N/mm^3	0.01 N/mm^3 vs. rigid [%]	0	0 N/mm^3 vs. rigid [%]	Rigid
N_1 (6592)	1.142	**97.50**	1.086	**92.78**	1.045	**89.21**	1.037	**88.58**	
N_3 (17304)	1.138	**97.18**	1.085	**92.66**	1.044	**89.15**	1.036	**88.47**	1.171
N_5 (28840)	**	**	1.090	**93.07**	1.053	**89.93**	1.036	**88.45**	

** Excluded from further analysis since the calculations were not completed after one month.

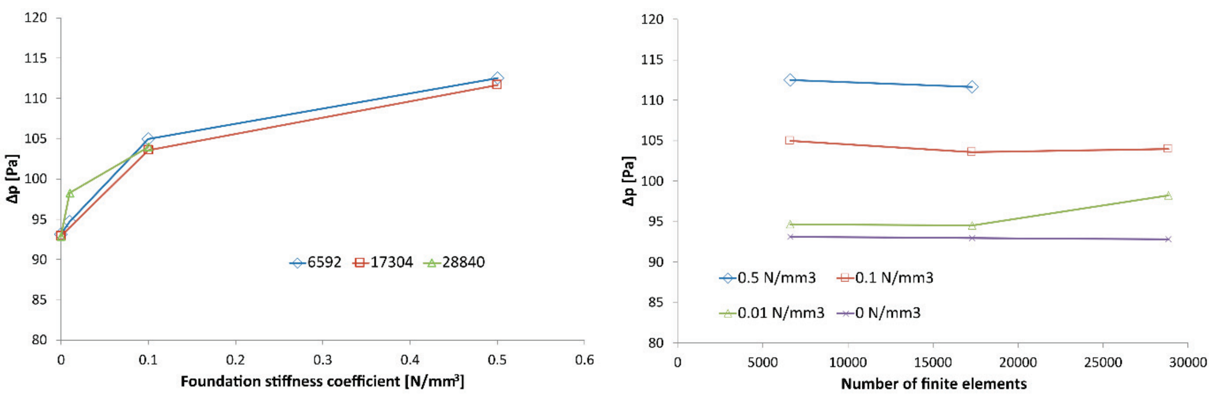

Fig. 11. Left: pressure drop vs. FS, right: pressure drop vs. number of elements in structure (E = 3 MPa, $\alpha = \beta = 0.01$); Δp = 116.8 Pa for rigid model; the case including FS = 0.5 N/mm^3 and mesh N_5 was excluded

Table 6. Pressure drop Δp [Pa] in FSI simulations for different values of the foundation stiffness coefficient and structural meshes (E = 3 MPa, $\alpha = \beta = 0.01$) compared to the rigid-wall approach

FSI									
N_i (number of elements)	0.5 N/mm^3	0.5 N/mm^3 vs. rigid [%]	0.1 N/mm^3	0.1 N/mm^3 vs. rigid [%]	0.01 N/mm^3	0.01 N/mm^3 vs. rigid [%]	0	0 N/mm^3 vs. rigid [%]	Rigid
N_1 (6592)	112.535	**96.35**	104.989	**89.89**	94.697	**81.08**	93.104	**79.71**	116.8
N_3 (17304)	111.694	**95.63**	103.593	**88.69**	94.528	**80.93**	92.932	**79.57**	
N_5 (28840)	**	**	103.976	**89.02**	98.242	**84.11**	92.847	**79.49**	

** Excluded from further analysis since the calculations were not completed after one month.

Furthermore, higher resilience, which is associated with lower FS, induces a larger pressure drop. As shown in Table 6, Δp obtained with the FSI approach for FS = 0.5/0.1/0.01/0 N/mm^3 is lower if compared to the rigid model, respectively, by about 4–5/11/16–19/ and 21%.

3.3. Dependence on damping

As mentioned above, the employment of Rayleigh damping in the FSI modelling requires the selection of mass (α) and stiffness (β) coefficients. However, the α and β are unknown. Therefore, various scenarios represented by different combinations of α and β were investigated in this study. In the first set of FSI simulations concerning damping, the equality of α and β in the wide range $\alpha = \beta = \{10^{-6}, 10^{-4}, 10^{-2}, 10^{-1}, 1, 10, 10^2\}$ was assumed, while the other parameters defining model's compliance were kept as constant (E = 3 MPa, FS = 0). The results obtained for $\alpha = \beta$ are presented in Fig. 12 (left) and Fig. 13 (left). High values of α and β have been suspected to give a non-physical response. This abnormality is associated with losing periodicity for $\alpha = \beta = \{1, 10, 10^2\}$, which is related to the rapid rise or fall on the presented charts. These cases are presented to show what happens if incorrect coefficients are set in FSI modelling. Maximal displacement and maximal von Mises stress had a similar trend and finally fell to zero for $\alpha = \beta = 100$, for which TAWSS increased up to 1.1664 Pa and Δp, having an irregular trend, reached 116.22 Pa. Thus, $\alpha = \beta = 100$ provided similar results as the rigid-wall case, in which TAWSS equal to 1.171 Pa and Δp equal to 116.8 Pa were obtained. A few combinations $\alpha = \beta$ were tested in a patient-specific case of the carotid bifurcation shown by Jodko et al. [14], where the magnitude of damping in the range of 0.0001–0.1 did not influence the hemodynamic results.

In the second test concerning damping, the mass damping was neglected ($\alpha = 0$) while the influence of the stiffness factor on the results was investigated for $\beta = \{10^{-6}, 10^{-4}, 10^{-2}, 10^{-1}, 1, 10, 10^2\}$. Such a test provided more regular trends of all the results than in the previous set, where $\alpha = \beta$. This is visible in Fig. 12 (right) and Fig. 13 (right), where maximal displacement, maximal von Mises stress, TAWSS, and Δp are constant and rational from the point of physics for $\beta = \{10^{-6}, 10^{-4}, 10^{-2}\}$, slightly change for $\beta = 0.1$, and, as in the previous set, become inappropriate for $\beta = \{1, 10, 10^2\}$ giving non-realistic results (Table 7).

The combination of $\alpha = 50$ and $\beta = 0.1$ was used by Zhu et al. [40] to carry out successful FSI simulations of the blood flow in the aorta and such a definition of damping was used in the second set of simulations, for which physical wall behaviour was observed

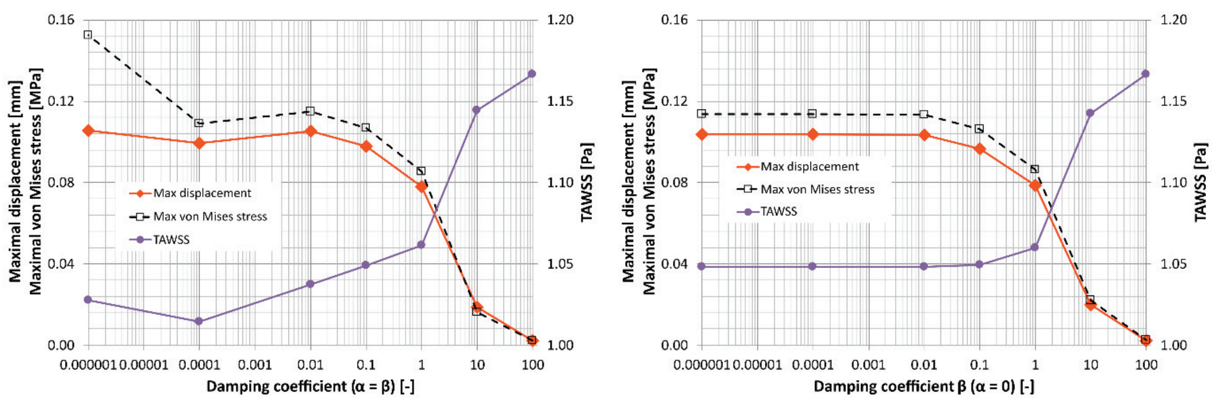

Fig. 12. Maximal displacement, max von Mises stress, and TAWSS vs. damping for $\alpha = \beta$ (left) and $\alpha = 0$ (right) (E = 3 MPa, FS = 0, structural mesh N_1), TAWSS = 1.171 Pa for rigid model

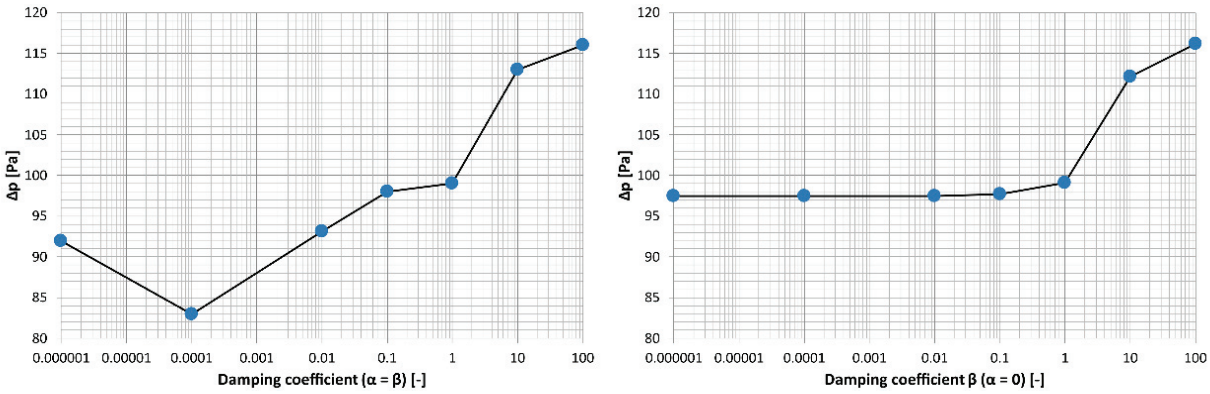

Fig. 13. dp vs damping for $\alpha = \beta$ (left) and $\alpha = 0$ (right) (E = 3 MPa, FS = 0, structural mesh N_1), dp = 116.8 Pa for rigid model

Table 7. Comparison of the computational time and the results obtained for the selected values of α and β coefficients, ∞ indicates the rigid-wall case

		Non-physical wall behaviour			Physical wall behaviour						Non-physical wall behaviour		
Mass damping [alpha]	∞	1	50	10^{-1}	50	0	0	0	0	0	0	0	0
Stiffness samping [beta]	∞	50	1	50	10^{-1}	0	10^{-6}	10^{-4}	10^{-2}	10^{-1}	1	10	100
TAWSS [Pa]	**1.171**	1.163	1.060	1.163	1.050	1.048	1.048	1.048	1.048	1.050	1.060	1.142	1.166
Δp [Pa]	**116.8**	115.7	99.11	115.7	97.71	97.49	97.49	97.50	97.51	97.71	99.11	112.1	116.2
Max displacement [mm]	–	0.0044	0.0787	0.0044	0.0967	0.1037	0.1037	0.1037	0.1035	0.0967	0.0787	0.0200	0.0023
Max von Mises stress [MPa]	–	0.0049	0.0865	0.0049	0.1061	0.1138	0.1138	0.1138	0.1135	0.1061	0.0865	0.0220	0.0025
Computational time	**33 min**	8 h 30 min	15 h 20 min	8 h 37 min	9 h 16 min	8 h 4 min	8 h 46 min	8 h 45 min	8 h 59 min	8 h 54 min	9 h 3 min	8 h 51 min	8 h 37 min

(Table 7). Thus, this study confirmed that the values assumed by Zhu et al. could provide physical results. An opposite situation (α = 0.1, β = 50), as well as, other combinations like (α = 50, β = 1) and (α = 1, β = 50), did not lead to successful and physically possible results. In the last cases, despite the cyclic boundary conditions, the model lost periodicity and none of the monitored parameters could represent the real-world situation.

4. Discussion

The performed mesh independence test was a kind of verification for the applied settings. When applicable, the findings were summarised and juxtaposed with *in vivo* and/or *in vitro* studies and other FSI modelling devoted to blood flow modelling to provide qualitative and quantitative validation. It is worth noting that some authors treated rigid wall simulations as a reference point, but other researchers considered FSI simulations as a base to calculate percentage differences.

4.1. Structural mesh displacement

As expected, the largest wall displacement (1.116–1.144 mm) was observed for the highly compliant model (E = 0.5 MPa, FS = 0) and decreased to (0.104–0.105 mm) when Young's modulus was raised to 3 MPa (Fig. 4). Similar maximal wall dilation was found in a carotid branch investigated in FSI analysis for the settings including the use of the linear model (E = 3 MPa) and low external support (FS = 0.1 N/mm^3) (14). Combinations (E = 3 MPa, FS = 0) and (E = 1 MPa, FS = 0) provided comparable results of maximal deformation (Fig. 4) as it was obtained in the FSI case of the hyperelastic carotid artery investigated by Kumar et al. [16], in which normal blood pressure was used to define an outlet boundary condition. It can be interpolated that using a combination (E = 2 MPa, FS = 0) would result in obtaining a similar maximal wall displacement, which was determined for the radial artery feeding AVF (0.62 mm) in the FSI study by Decorato et al. [7]. A similar maximal displacement (0.6 mm) was obtained in the radial artery supplying blood to AVF by Guess [8], however, the authors indicated that the reason for such a large displacement is associated with no-prestressing conditions. For the case where E = 3 MPa and FS = 0.5, the maximal dilation is much lower (0.03–0.04 mm). Additionally, in the case of the mesh N_1, the changes in displacement lost the periodicity of the pressure boundary condition, which can be related to a natural frequency. However, such a low deformation is in good agreement with a set of data that were shown by McGah et al. [23], who in radial artery feeding AVF obtained peak *in vivo* displacement at the level of 45.7 ± 17.3 μm (mean ± SD, for three cardiac cycles). In an *in vivo* study of six radial arteries feeding 12-week AVFs, Corpataux et al. also did not observe significant changes in the diameter within the cardiac cycle, which did not exceed 0.056 mm (1.5% of the mean diameter) [5]. Nevertheless, only six patients were included in that study, and the ultrasound method was used in measurements by the authors. Thus, more *in vivo* measurements of arterial displacement, which would be combined with FSI simulations using reverse engineering, are needed to determine the settings that could describe the wall stiffness and LCT's behaviour in an appropriate manner.

4.2. Von Mises stress

For the first set of data, the purpose of which was to compare different Young's moduli (3–0.5 MPa), the maximal von Mises stress was obtained in the range of 0.1150–0.1775 MPa (for all meshes N_1–N_5). This corresponds to the results obtained in the patient-specific FSI study of carotid blood flow for E = 0.5–1 MPa and external support defined by FS = 0.1–0.2 N/mm^3 [14]. In the FSI analysis of a patient-specific and hyperelastic case of AVF, Decorato et al. found the distribution of the maximum component of the principal stresses (representing the Cauchy stress), which fell in the range of 0.0055–0.007 MPa within the arterial wall, with a space-averaged value of 0.0057 MPa, however, these results cannot be directly compared to von Mises stress. One has to remember that the isotropic, linear, and homogenous material model representing the arterial wall was assumed in this study. Thus, determining von Mises stress can be used here rather for a qualitative comparison of cases, and not as a basis for quantitative analysis. On the other hand, *in vivo* validation of the stress obtained numerically is challenging due to the lack of bio-extensometers that could be used for stress measurements. It is worth mentioning that estimating the stress in the arterial wall with modern ultrasound devices is burdened with errors related to the methodology and simplifications included in the mathematical models employed by the software [21].

4.3. TAWSS

As shown in Table 3, in the most resilient model presented here (E = 0.5 MPa, FS = 0), TAWSS decreased by about 45% compared to the rigid model. This difference was lowered to around 12% for E = 3 MPa when no external support is applied, or even 3%, if E = 3 MPa and if the elastic support is defined by FS = 0.5 N/mm^3 (Table 5). It has been shown for a patient-specific case of a carotid branch that the difference in the area-averaged WSS obtained between rigid-wall and FSI approach (for E = 1 MPa, no external support) can oscillate in the range 13–35% within the cardiac cycle [14]. A decrease in WSS was also observed in a qualitative comparison based on an FSI study of blood flows in both stenosed and normal carotid branches, which were compared to rigid-walled analogous models [31]. Similarly, in the FSI study of the pulmonary artery, Liu et al. [17] found that the rigid model overpredicts the averaged WSS of about 52.6% in comparison to the compliant one. McGah et al. [23] concluded that, when compared to FSI simulations of blood flow within AVF, the rigid wall assumption is burdened with uncertainty associated with overestimating TAWSS by up to 10, 20 and even 50%, respectively, in the proximal vein, in the proximal artery, and locally in the anastomosis connecting these two first blood vessels. Decorato et al. found an overestimation of maximal WSS (15%) and peak velocity (20%) in a rigid model of a radio-cephalic AVF when compared to the analogous rigid-walled case [7]. The last findings are consistent with the observations of Guess [8], who found that maximal WSS can be overestimated by 12% in the rigid model. In another study, Decorato et al. [6] observed that TAWSS was larger in the rigid model of a brachio-cephalic AVF compared to the FSI case (10% in the cephalic vein and 13.1% in the proximal brachial artery). Reymond et al. [30] observed a rise of about 43% in maximal WSS in the aorta when the results of the rigid-wall simulation were compared to FSI calculations. Therefore, it allows us to state that the resulting range of the stiffness level, coming from wall elasticity and the tissue surrounding arteries, was in this study wide enough to capture almost all the discrepancies between rigid and resilient models, which have been found in the above-mentioned studies.

An interesting method comparing rigid and distensible arterial models was presented by Lopes et al. [20], showing carotid hemodynamics, and Zhu et al. [40], who investigated two cases of surgically repaired aortic dissections. As low TAWSS is prone to increase the risk of atherosclerotic plaque and clot formation, these authors determined the percentage of the total area where TAWSS is lower than the threshold value, which was 0.4 Pa in the carotid bifurcation and 0.2 Pa in the aorta case. In the first example, the difference in the areas exposed to low TAWSS between the rigid-walled and the FSI simulation (for which E = 1.106 MPa) was around 3%. In the second example, such low-wall shear zones were by about 180% (case 1) and 411% (case 2) larger in FSI simulations than in rigid-wall models (the linear material model was used with E = 1.08 MPa). However, when Young's modulus of the wall was doubled, the circumferentially determined TAWSS changed by around 5.6%. In the presented study, wall compliance played a more significant role.

4.4. Pressure drop

This simple numerical experiment shows that wall compliance considerably affects the pressure conditions. In all the presented cases, the same normal blood pressure waveform was assumed as the outlet boundary condition. The magnitude of the inlet pressure depends not only on the outlet pressure but, as a product of calculations, hinges also on the velocity profile applied to the inlet and the wall resilience. Thus, the pressure drop between the inlet and the outlet was calculated to compare the results.

As shown in Table 4, in the highly compliant model (E = 0.5 MPa, FS = 0), Δp was decreased by about 59–66% when compared to the rigid case. This difference was lowered to around 21% for E = 3 MPa and FS = 0, or even 4–5%, for E = 3 MPa and FS = 0.5 N/mm^3 (Table 6). This implies that, as giving similar results to the rigid-wall case, the last case could be replaced by a rigid-walled simulation if the error of 5% is acceptable. Carrying out an FSI simulation for relatively stiff walls would be associated with wasting computational powers and the time which is necessary to perform such a simulation (4 d 20 h 52 min for FSI vs. 33 min for rigid-walled in the case of the simplest structural mesh N_1, Table 2). In such a case, the assumption of wall rigidity would be satisfactory.

However, determining patient-specific, exact material properties of the living arterial tissue and LCT is still challenging, as the resulting stiffness is unknown. Further, available material models, which are based on tensile mechanical tests, including samples that have been prepared and taken out of the human body, seem controversial. Therefore, more *in vivo* studies must be done to obtain more data which could be implemented in the developed numerical studies to describe the mechanics of living soft tissue. It is worth mentioning that a good agreement between the results regarding a pressure drop in AVF obtained in an FSI study and experimental measurements done in a compliant phantom was presented in [15]. In another *in vitro* study of the blood flow through AVF, the authors raised the necessity of using compliant models in experimental work [1]. However, the authors did not take into account the pressure condition, which, contrary to the observations by others, probably led them to the conclusion that flow velocity is higher in the resilient model than in the rigid one. Lowering the pressure in the fluid domain was observed in the FSI study of the carotid artery when the resilience of the wall was increased [14].

4.5. Limitations

As numerous patient-specific FSI studies have been presented in the literature, due to the wide range of factors affecting wall compliance, the presented idealised model can be treated as a representative example of the high-flow artery. However, a one-layered, isotropic and linear material model was employed for the structure to carry out FSI calculations on the available PC station in a reasonable time. Interestingly, some authors argue that using linear models provides a proper approximation for relatively small deformations [37], while others consider linear material behaviour to be an unacceptable simplification [35]. Newtonian rheological model of blood was used here, however, the blood flows in large arteries are characterised by a high-shear environment, in which blood viscosity tends to be constant. The arbitrarily selected values of the foundation stiffness coefficient were used to define the mechanical response of LCT, but the real magnitude of LCT's reaction remains unknown. Further, although Rayleigh damping was used here with wide-range settings, this approach could lead to overdamping. Using lower timesteps in high-frequency analysis could reveal wall vibrations that were confirmed in a monolithic approach [35]. No anti-prestressing condition was used here, which led to high wall dilation in a few cases. Prestressing occurs naturally in arterial walls to counteract the static and hydraulic forces generated by the blood, even in the end-diastolic phase. Prestressing is a challenging limitation in patient-specific FSI studies since arterial geometry, obtained with ultrasonography, angio-CT, or MRI, is always acquired in a prestressed state of homeostasis. Therefore, neglecting this phenomenon could raise differences between rigid-walled and FSI approaches [33].

5. Conclusions

A simplified, but representative, FSI model was used to investigate the significance of blood vessel wall compliance defined by E (0.5–3 MPa) and the response of the LCT tissue surrounding the artery described by FS (0–0.5 N/mm^3). Additionally, cushioning effects in a high-flow artery were analysed. The results obtained were compared to other FSI studies on blood flow.

Despite the anti-prestressing condition being neglected here, the obtained results regarding wall dilation, WSS, and inlet/outlet Δp fall in the physiological range or are comparable to a few advanced multi-parameter FSI studies for all the proposed combinations (E, FS). However, the total resilience, resulting from the defined E and FS, should be validated by patient-specific cases individually with *in vivo* measurements of the arterial wall displacement. The newly developed diagnostic method, arterial elastography, is promising in providing a valuable validation. Then, reverse engineering could help to find the best pairs (E, FS) describing the wall behaviour during a heart operation. Otherwise, FSI simulations aiming at patient-specific blood flow modelling will still be based on numerous guesses. Three numerical grids (N_1, N_3, N_5) representing the structural domain were compared. The influence of the structural mesh density on the maximal displacement of the wall, TAWSS, and Δp was negligible. Thus, it can be stated that, as far as von Mises stress is not investigated, coarse structural meshes could be used. Lower structural mesh fidelity allows one to complete the FSI simulations much faster without affecting hemodynamic parameters. Determining von Mises stress is more difficult and needs further verification due to its sensitivity to structural mesh density, which was also shown by Liu and Fletcher [18]. Further, validating von Mises stress seems more difficult due to the complexity of *in vivo* measurements of this parameter. Analysis of cushioning effects, represented here by Rayleigh damping, leads to the conclusion that neglecting the mass damping coefficient and keeping the stiffness damping coefficient lower than 10^{-2} allows one to perform an FSI simulation successfully without affecting hemodynamic parameters. Different combinations (α, β) may lead to abnormalities and non-physical results. Dealing with overdamping may be especially important in vortex-induced analyses of real-world engineering problems, e.g., pipelines, where wall vibrations can lead to malfunctions.

Summarizing, the FSI approach is worth considering as wall compliance leads to differences in hemodynamic parameters obtained on the fluid side of the FSI interface if compared to the rigid-wall assumption. However, the FSI method is time-consuming for those without access to high-speed computers and developed commercial or in-house software. Therefore, the use of FSI in clinical practice or research remains limited, especially in patient-specific studies that require the development of complex geometric models. Rigid wall simulations will still be used in qualitative analyses or preliminary studies to identify key flow characteristics or areas where hemodynamic parameters reach extreme values. Nevertheless, peak and time-averaged values of the flow parameters are overestimated when wall compliance is omitted; thus, FSI should be considered in the design of new cardiovascular devices such as stents, flow diverters, and drug delivery systems as well as in studies aimed at predicting disease, such as the development of stenosis or aneurysm rupture. Finally, as the relative errors between rigid-walled and FSI simulations depend on the model's geometry, these discrepancies should always be determined.

Acknowledgements

This work was financially supported by the Polish National Agency for Academic Exchange (the Bekker programme, PPN_BEK_2020_1_00115). The author thanks Prof. Tracie Barber from UNSW, Sydney, Australia, for the first critical review of the manuscript.

References

[1] ALAM N., NEWPORT D., *Influence of Wall Compliance on the Flow Patterns in a Patient-Specific Brachio-Cephalic Arterio-Venous Fistula*, Biomechanics, 2022, 2 (2), 158–173.

[2] BATEMAN A.R., LECHNER-SCOTT J., BATEMAN G.A., RAMADAN S., BARBER T., *Computational Fluid Dynamic Simulation of the Cerebral Venous System in Multiple Sclerosis and Control Patients: Are Hemodynamic Variances Evident in Multiple Sclerosis?*, IEEE Trans. Biomed. Eng., 2024.

[3] BERGERSEN A., SLYNGSTAD A., GJERTSEN S., SOUCHE A., VALEN-SENDSTAD K., *turtleFSI: A Robust and Monolithic FEniCS-based Fluid-Structure Interaction Solver*, J. Open Source Softw., 2020, 5 (50), 2089.

[4] BUKALA J., KWIATKOWSKI P., MALACHOWSKI J., *Numerical analysis of crimping and inflation process of balloon-expandable coronary stent using implicit solution*, Int. J. Numer. Method Biomed. Eng., 2017, 33 (12).

[5] CORPATAUX J.M., *Low-pressure environment and remodelling of the forearm vein in Brescia-Cimino haemodialysis access*, Nephrology Dialysis Transplantation, 2002, 17 (6), 1057–1062.

[6] DECORATO I., KHARBOUTLY Z., LEGALLAIS C., SALSAC A.V., *Numerical study of the influence of wall compliance on the haemodynamics in a patient-specific arteriovenous fistula*, Comput. Methods Biomech. Biomed. Engin., 2011, 14 (Suppl. 1), 121–123.

[7] DECORATO I., KHARBOUTLY Z., VASSALLO T., PENROSE J., LEGALLAIS C., SALSAC A.V., *Numerical simulation of the fluid structure interactions in a compliant patient-specific arteriovenous fistula*, Int. J. Numer. Method Biomed. Eng., 2014, 30 (2), 143–159.

[8] GUESS W., *Fluid-structure interaction modelling of a patient-specific arteriovenous access fistula*, Thesis. University of Cape Town, 2016.

[9] GUNASEKERA S., NG O., THOMAS S., VARCOE R., DE SILVA C., BARBER T., *Tomographic PIV analysis of physiological flow conditions in a patient-specific arteriovenous fistula*, Exp. Fluids, 2020, 61 (12), 253.

[10] GUNASEKERA S., NG O., THOMAS S., VARCOE R., DE SILVA C., BARBER T., *Impact of juxta-anastomotic stent implantation on the haemodynamics within a single representative patient AVF*, Int. J. Heat Fluid Flow, 2021, 92, 108874.

[11] HEIL M., *An efficient solver for the fully coupled solution of large-displacement fluid-structure interaction problems*, Comput. Methods Appl. Mech. Eng., 2004, 193 (1–2), 1–23.

[12] JIANG M.X., KHAN M.O., GHOBRIAL J., ROGERS I.S., PETTERSSON G.B., BLACKSTONE E.H. et al., *Patient-specific fluid–structure simulations of anomalous aortic origin of right coronary arteries*, JTCVS Tech., 2022, 13, 144–162.

[13] JODKO D., BARBER T., *Fluid–structure interaction in a follow-up study of arterio-venous fistula maturation*, Sci. Rep., 2024, 14 (1), 1–20.

[14] JODKO D., JECKOWSKI M., TYFA Z., *Fluid structure interaction versus rigid-wall approach in the study of the symptomatic stenosed carotid artery: Importance of wall compliance and resilience of loose connective tissue*, Int. J. Numer. Method Biomed. Eng., 2022, 38 (8), e3630.

[15] JODKO D., PALCZYNSKI T., REOROWICZ P., MIAZGA K., OBIDOWSKI D., JOZWIK K., *Determination of a pressure drop in the arteriovenous fistula with fluid structure interaction simulations and in vitro methods*, ASME International Mechanical Engineering Congress and Exposition, Proceedings (IMECE), 2017.

[16] KUMAR N., KHADER S.M.A., PAI R., KHAN S.H., KYRIACOU P.A., *Fluid structure interaction study of stenosed carotid artery considering the effects of blood pressure*, Int. J. Eng. Sci., 2020, 154, 103341.

[17] LIU J., YANG W., LAN I.S., MARSDEN A.L., *Fluid-structure interaction modeling of blood flow in the pulmonary arteries using the unified continuum and variational multiscale formulation*, Mech. Res. Commun., 2020, 107, 103556.

[18] LIU X., FLETCHER D.F., *Verification of fluid-structure interaction modelling for wave propagation in fluid-filled elastic tubes*, J. Algorithm Comput. Technol., 2023, 17, 1–13.

[19] LIU Y., ZHENG Y., PITRE J., WEITZEL W., BULL J., SHIH A., *Manufacturing and Computational Fluid Dynamics Modeling of a Patient-Specific Fistula Model* – MSEC2017-3002 [Internet]. 2017. Available from: https://asmedigitalcollection.asme.org/MSEC/proceedings-abstract/MSEC2017/50756/V004T05A011/268670

[20] LOPES D., PUGA H., TEIXEIRA J.C., TEIXEIRA S.F., *Influence of arterial mechanical properties on carotid blood flow: Comparison of CFD and FSI studies*, Int. J. Mech. Sci., 2019, 160, 209–218.

[21] LUO X., DU L., LI Z., *Ultrasound assessment of tensile stress in carotid arteries of healthy human subjects with varying age*, BMC Med. Imaging., 2019, 19 (1), 93.

[22] MANCINI V., BERGERSEN A.W., VALEN-SENDSTAD K., SEGERS P., *Computed poststenotic flow instabilities correlate phenotypically with vibrations measured using laser doppler vibrometry: Perspectives for a promising in vivo device for early detection of moderate and severe carotid stenosis*, J. Biomech. Eng., 2020, 142 (9).

[23] MCGAH P.M., LEOTTA D.F., BEACH K.W., ALISEDA A., *Effects of wall distensibility in hemodynamic simulations of an arteriovenous fistula*, Biomech. Model Mechanobiol., 2014, 13 (3), 679–695.

[24] MUHA B., ČANIĆ S., *Existence of a solution to a fluid-multi-layered-structure interaction problem*, J. Differ. Equ., 2014, 256 (2), 658–706.

[25] NAGY J., FENZ W., THUMFART S., MAIER J., MAJOR Z., STEFANITS H. et al., *Fluid structure Interaction analysis for rupture risk assessment in patients with middle cerebral artery aneurysms*, Sci. Rep., 2025, 15 (1), 1965.

[26] NIEMANN A.K., UDESEN J., THRYSOE S., NYGAARD J.V., FRÜND E.T., PETERSEN S.E. et al., *Can sites prone to flow induced vascular complications in a-v fistulas be assessed using computational fluid dynamics?*, J. Biomech., 2010, 43 (10), 2002–2009.

[27] PAPADAKIS G., RASPAUD J., *Wave propagation in stenotic vessels; theoretical analysis and comparison between 3D and 1D fluid–structure-interaction models*, J. Fluids Struct., 2019, Jul 1, 88, 352–366.

[28] PEIRLINCK M., COSTABAL F.S., YAO J., GUCCIONE J.M., TRIPATHY S., WANG Y. et al., *Precision medicine in human heart modeling: Perspectives, challenges, and opportunities*. Vol. 20, Biomechanics and Modeling in Mechanobiology, Springer Science and Business Media Deutschland GmbH, 2021. p. 803–831.

[29] RAHMAN M.H., GUPTA C., *Computation of Rayleigh damping coefficient of a rectangular submerged floating tunnel (SFT)*, SN Appl. Sci., 2020, 2 (5), 936.

[30] REYMOND P., CROSETTO P., DEPARIS S., QUARTERONI A., STERGIOPULOS N., *Physiological simulation of blood flow in the aorta: Comparison of hemodynamic indices as predicted by 3-D FSI, 3-D rigid wall and 1-D models*, Med. Eng. Phys., 2013, 35 (6), 784–791.

[31] REZAZADEH M., OSTADI R., *Numerical simulation of the wall shear stress distribution in a carotid artery bifurcation*, Journal of Mechanical Science and Technology, 2022, 36 (10), 5035–5046.

[32] SANDEEP S., SHINE S.R., *Effect of stenosis and dilatation on the hemodynamic parameters associated with left coronary artery*, Comput. Methods Programs Biomed., 2021, 204, 106052.

[33] SCHOENBORN S., LORENZ T., KUO K., FLETCHER D.F., WOODRUFF M.A., PIROLA S. et al., *Fluid-structure interactions of peripheral arteries using a coupled in silico and in vitro approach*, Comput. Biol. Med., 2023, 165.

[34] SIVANESAN S., HOW T.V., BLACK R.A., BAKRAN A., *Flow patterns in the radiocephalic arteriovenous fistula: An in vitro study*, J. Biomech., 1999, 32 (9), 915–925.

[35] SOLIVERI L., BRUNEAU D., RING J., BOZZETTO M., REMUZZI A., VALEN-SENDSTAD K., *Toward a physiological model of vascular wall vibrations in the arteriovenous fistula*, Biomech. Model Mechanobiol., 2024, 23, 1741–1755.

[36] SONNTAG S.J., KAUFMANN T.A.S., BÜSEN M.R., LAUMEN M., LINDE T., SCHMITZ-RODE T. et al., *Simulation of a pulsatile total artificial heart: Development of a partitioned Fluid Structure Interaction model*, J. Fluids Struct., 2013, 38, 187–204.
[37] TORII R., OSHIMA M., KOBAYASHI T., TAKAGI K., TEZDUYAR T.E., *Influence of wall elasticity in patient-specific hemodynamic simulations*, Comput. Fluids, 2007, 36 (1), 160–8.
[38] WIESE P., NONNAST D.B., *Colour doppler ultrasound in dialysis access*, Nephrology Dialysis Transplantation, 2004, 19 (8), 1956–1963.
[39] ZHANG Y., CHEN D., QIAN H., CHEN Z., FAN F., KHOO B.C., *An efficient partitioned framework to couple Arbitrary Lagrangian–Eulerian and meshless vector form intrinsic finite element methods for fluid-structure interaction problems with deformable structures*, Appl. Math. Model, 2024, 130, 536–560.
[40] ZHU Y., MIRSADRAEE S., ROSENDAHL U., PEPPER J., XU X.Y., *Fluid-Structure Interaction Simulations of Repaired Type A Aortic Dissection: a Comprehensive Comparison With Rigid Wall Models*, Front. Physiol., 2022, Jun 14, 13.